Journal of Materials Chemistry A

Accepted Manuscript

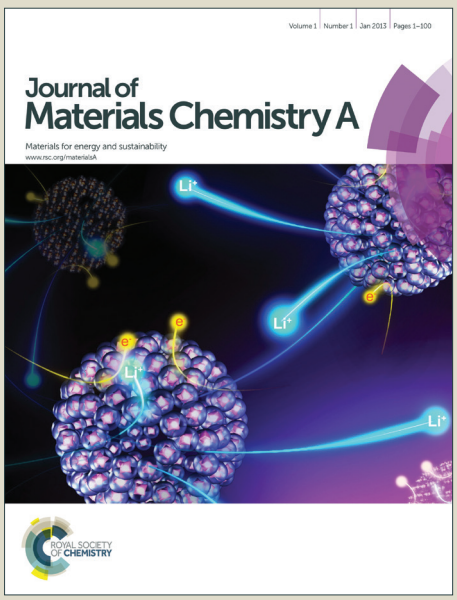

ROYAL SOCIETY OF CHEMISTRY

www.rsc.org/materialsA

Correlation between fast oxygen kinetics and enhanced performance in Fe doped layered perovskite cathode for solid oxide fuel cells

Areum Jun,[a] Seonyoung Yoo,[a] Young-Wan Ju,[a] Junji Hyodo,[b] Sihyuk Choi,[a] Hu Young Jeong,[c] Jeeyoung Shin,[d] Tatsumi Ishihara,[b] Tak-hyoung Lim,[e,*] and Guntae Kim[a,*]

[a] *Department of Energy Engineering, Ulsan National Institute of Science and Technology (UNIST), Ulsan, 689–798, Korea*

[b] *International Institute for Carbon Neutral Energy Research, Kyushu University, Fukuoka 819-0395, Japan*

[c] *UNIST Central Research Facilities and School of Mechanical and Advanced Materials Engineering, UNIST, Ulsan, 689–798, Korea*

[d] *Department of Mechanical Engineering, Dong-Eui University, Busan 614-714, Korea*

[e] *Hydrogen & Fuel Cell Department, Korea Institute of Energy Research (KIER), Daejeon 305-343, Korea*

Abstract

Many researchers have recently focused on layered perovskite oxides as cathode materials for solid oxide fuel cells because of their much higher chemical diffusion and surface exchange coefficients relative to those of ABO_3-type perovskite oxides. Herein, we study the catalytic effect of Fe doping in $SmBa_{0.5}Sr_{0.5}Co_2O_{5+\delta}$ for the oxygen reduction reaction (ORR) and investigate the optimal Fe substitution through an analysis of the structural characteristics, electrical properties, redox properties, oxygen kinetics, and electrochemical performance of $SmBa_{0.5}Sr_{0.5}Co_{2-x}Fe_xO_{5+\delta}$ (x = 0, 0.25, 0.5, 0.75, and 1.0). The optimal Fe substitution, $SmBa_{0.5}Sr_{0.5}Co_{1.5}Fe_{0.5}O_{5+\delta}$, enhanced the performance and redox stability remarkably and also exhibited satisfactory electrical properties and electrochemical performance due to its fast oxygen bulk diffusion and high surface kinetics under typical fuel cell operating conditions. The results suggest that $SmBa_{0.5}Sr_{0.5}Co_{1.5}Fe_{0.5}O_{5+\delta}$ is a promising cathode material for intermediate-temperature solid oxide fuel cells (IT-SOFCs).

Keywords: Solid oxide fuel cells (SOFC); layered perovskite; cathode; electrochemical performance

** Corresponding author: E-mail: gtkim@unist.ac.kr, Fax: +82 52 217 2909*

E-mail: ddak@kier.re.kr, Fax: +82 42 860 3297

Introduction

Solid oxide fuel cells (SOFCs), which directly convert the chemical energy of a fuel gas into electrical energy, are attractive power generation systems with high energy conversion efficiency, environmental benefits, and greater fuel flexibility.[1-3] However, in spite of a number of advantages compared with conventional power generation systems, they accompany critical problems such as high cost, thermal stress, and material compatibility challenges due to the high operating temperature (800-1000 ^{o}C).[4] For many years, the development of SOFCs has focused on lowering the operating temperature to an intermediate range (500-700 ^{o}C). By lowering the device operating temperature, a wider range of materials can be used to improve the material compatibility and the practical applicability. Developing cathode materials with high electrocatalytic activity for the oxygen reduction reaction (ORR) is also a vital step toward successful operation at intermediate temperature since lower operating temperature causes slow oxygen reduction kinetics and high over-potential at the cathode.[5]

In this regard, mixed ionic electronic conducting (MIECs) cathodes, which exhibit simultaneous electronic and ionic conduction,[6] have received considerable attention for application to intermediate-temperature solid oxide fuel cells (IT-SOFCs). MIEC cathode materials show high performance at the intermediate temperature range, since the oxygen reduction reaction occurs not only at the triple-phase boundary (TPB) between the electrolyte, cathode, and gas phase but also at the two phase boundary between the electrode and gas phase.[7,8]

Among MIECs, layered perovskite oxides described with the general formula $AA'B_2O_{5+\delta}$, have recently been studied by numerous research groups based on their much higher chemical diffusion and surface exchange coefficients relative to those of ABO_3-type perovskite oxides such as $Ba_{0.5}Sr_{0.5}Co_{0.8}Fe_{0.2}O_{3-\delta}$,[9] $La_{0.6}Sr_{0.4}Co_{0.2}Fe_{0.8}O_{3-\delta}$,[10] $Pr_{1-x}Sr_xCoO_{3-\delta}$,[11] and $Sm_{0.5}Sr_{0.5}CoO_3$.[12] In particular, the $LnBaCo_2O_{5+\delta}$, cobalt containing layered perovskite oxides, have stacking layers of …[LnO_δ]-[CoO_2]-[BaO]-[CoO_2]…. According to modeling results obtained by the authors using density functional theory (DFT) in a previous study, the layered structure possesses pore channels in the [Ln-O] and [Co-O] planes that provide fast paths for oxygen transport, which in turn enhances the kinetics

of surface oxygen exchange.[13]

Several researchers have examined the effects of ion substitution on the characteristics of $LnBaCo_2O_{5+\delta}$. For example, Sr substitution of Ba enhances the electrochemical characteristics owing to the higher conductivity and higher oxygen content of the Sr doped layered perovskite oxides, which are considered to be favorable to the ORR.[14] Various transition metal ions also have been introduced into the B-site such as Mn, Fe, Ni, and Cu.[15-18] In particular, Fe substitution of Co improves the oxygen ion diffusivity, ORR activity, and stability of the cathodes due to increased 3d metal-oxygen bonding energy and decreased thermal expansion.[19]

In a previous study, we investigated the effects of strontium doping on $SmBa_{1-x}Sr_xCo_2O_{5+\delta}$ and reported that the electrochemical performance of $SmBa_{0.5}Sr_{0.5}Co_2O_{5+\delta}$ is remarkably high.[14] Herein, we focus on the catalytic effect of Fe doping of $SmBa_{0.5}Sr_{0.5}Co_2O_{5+\delta}$ for the ORR and optimize the amount of Fe substitution through an investigation of the structural characteristics, electrical properties, redox properties, oxygen kinetics, and electrochemical performance of $SmBa_{0.5}Sr_{0.5}Co_{2-x}Fe_xO_{5+\delta}$ (x = 0, 0.25, 0.5, 0.75, and 1.0) in relation to its application as an IT-SOFC cathode material.

Experimental

Cathode materials $SmBa_{0.5}Sr_{0.5}Co_{2-x}Fe_xO_{5+\delta}$ (x = 0, 0.25, 0.5, 0.75, and 1.0) were synthesized by the Pechini method. Stoichiometric amounts of $Sm(NO_3)_3 \cdot 6H_2O$ (Aldrich, 99+%, metal basis), $Ba(NO_3)_2$ (Aldrich, 99+%), $Sr(NO_3)_2$ (Aldrich, 99+%), $Co(NO_3)_2 \cdot 6H_2O$ (Aldrich, 98+%), and $Fe(NO_3)_2 \cdot 9H_2O$ (Aldrich, 99+%) were dissolved in distilled water to form an aqueous mixed solution with a proper amount of citric acid. An adequate amount of ethylene glycol was added into the beaker after the mixture was dissolved. After a viscous resin was formed, the mixture was heated to roughly 250 ^oC in air, followed by combustion to form powders, which were calcined at 600 ^oC for 4 h and ball-milled in acetone for 24 h. For measurement of the electrical conductivity and coulometric titration, the powder was pressed into pellets and then sintered in air at 1150 ^oC for 12 h. For the cathode slurry, $SmBa_{0.5}Sr_{0.5}Co_{2-x}Fe_xO_{5+\delta}$ and $Ce_{0.9}Gd_{0.1}O_{2-\delta}$ (GDC) powders were thoroughly mixed

together at a weight ratio of 6:4 and the mixed powders were then blended with an organic binder (Heraeus V006) to form slurries.

The crystalline structure of $SmBa_{0.5}Sr_{0.5}Co_{2-x}Fe_xO_{5+\delta}$ was characterized by using an X-ray diffractometer (Rigaku diffractometer, Cu Kα radiation). The powder pattern and lattice parameters were analyzed by Rietveld refinement using the GSAS program. $SmBa_{0.5}Sr_{0.5}Co_{1.5}Fe_{0.5}O_{5+\delta}$(SBSCF50) was also analyzed using an in situ X-ray diffractometer (Bruker AXS D8 Advance diffractometer, Cu Kα radiation) to determine the phase stability in air from 100 to 800 ^oC. The microstructures of the $SmBa_{0.5}Sr_{0.5}Co_{2-x}Fe_xO_{5+\delta}$ composites and cross sections of single cells were investigated using field emission scanning electron microscopy (Nova Nano SEM, FEI, USA). A thermogravimetric analysis (TGA) was performed using a thermogravimetric analyzer (SDT-Q600, TA Instruments, USA) from 100 to 900 ^oC with a heating/cooling rate of 2 $^oC\ min^{-1}$ in air. The initial oxygen content values at room-temperature were determined by iodometric titration.

The electrical conductivities of $SmBa_{0.5}Sr_{0.5}Co_{2-x}Fe_xO_{5+\delta}$ samples were measured by a four-terminal DC arrangement technique. The current and the voltage were recorded by a BioLogic Potentiostat from 100 to 750 ^oC at intervals of 50 ^oC in air.

Coulometric titration was used to accurately quantify the oxidation/reduction state of the $SmBa_{0.5}Sr_{0.5}Co_{2-x}Fe_xO_{5+\delta}$ specimens as a function of $p(O_2)$. The coulometric titration rig was mainly composed of an YSZ tube with Ag-paste electrodes plastered on both sides, a setup that has been described sufficiently elsewhere.[20] The sample was considered to be equilibrated when the potential varied in a range of less than 1 mV per hour. Oxygen nonstoichiometry was decided through this process at 700 ^oC over a wide range of oxygen partial pressure. The oxygen partial pressure dependence of the electrical conductivity was also measured by the four-probe DC method with a BioLogic Potentiostat on sintered bars of $SmBa_{0.5}Sr_{0.5}Co_{2-x}Fe_xO_{5+\delta}$.

Impedance spectroscopy of $SmBa_{0.5}Sr_{0.5}Co_{2-x}Fe_xO_{5+\delta}$ was carried out using a symmetric cell. The GDC powder was pressed into pellets and sintered at 1350 ^oC for 4 h in air to obtain a ~ 0.6 mm-thick electrolyte substrate. Slurries of the $SmBa_{0.5}Sr_{0.5}Co_{2-x}Fe_xO_{5+\delta}$-GDC composite were screen-printed

onto both sides of the dense GDC electrolyte to form a symmetrical cell, which was then heated at 950 °C for 4 h. Silver paste was used as the current collector for the electrodes.

A NiO-GDC anode-supported cell was fabricated to measure the electrochemical performance of $SmBa_{0.5}Sr_{0.5}Co_{2-x}Fe_xO_{5+\delta}$. The NiO-GDC cermet anode was prepared by a mixture of nickel oxide, GDC, and starch at a weight ratio of 6:4:1.5 after being ball-milled in ethanol for 24 h. The GDC electrolyte was pressed onto the pelletized disk of the NiO-GDC cermet anode, followed by co-sintering at 1350 °C for 5 h. Cathode slurries were applied onto the surface of the GDC electrolyte layer by screen printing and were finally sintered at 950 °C for 4 h in air. The electrolyte and cathode thickness of a single cell were both about ~ 20 μm with a 500 μm thick anode. For the single-cell performance test, Ag wires were attached at both electrodes of the single cell using Ag paste as a current collector. The single cell was fixed on an alumina tube using a ceramic adhesive (Aremco, Ceramabond 552). Humidified hydrogen (3 % H_2O) was supplied as fuel through a water bubbler with a flow rate of 100 mL min^{-1} and ambient air was used as an oxidant during single cell tests. *I-V* curves and impedance spectra were examined using a BioLogic Potentiostat at operating temperature from 500 to 650 °C. Impedance spectra were recorded under OCV in a frequency range of 1 mHz to 500 kHz with AC perturbation of 14 mV from 500 to 650 °C.

Isotope oxygen exchange was carried out using a closed circulation system with >96 % $^{18}O_2$. The concentration of $^{18}O_2$ in the gas phase was measured by a mass analyzer (Anelva, M-100-QA-F). The measured samples were polished using diamond paste and the final diameter of diamond paste was 0.25 μm. Natural abundance O_2 under pressure of 200 mbar was introduced into the system with a measured sample, and the sample was heated to 590 °C. The measured samples were annealed for more than ten times longer than the isotope oxygen exchanging time.[21] The sample was cooled to the room temperature, and residual oxygen was removed from the system. Subsequently, $^{18}O_2$ at pressure of 200 mbar was introduced for oxygen exchange. The sample was then heated rapidly to room temperature. After isotope oxygen exchanging for 40 min, the sample was quenched to room temperature. The obtained sample was cut into a bar shape, and the cut surface was polished by diamond paste. The isotope oxygen diffusion profile was obtained by secondary ion mass

spectrometry (SIMS) using an ATOMICA 4100 quadrupole-base analyzer, with the line-scan mode at the cross section of the sample using a cesium ion primary source (Cs^+) at 10 keV. The tracer diffusion coefficient (D^*) and the oxygen surface exchange coefficient (k) were estimated by fitting to the semi-infinite diffusion model.[22]

Results and Discussion

XRD patterns of $SmBa_{0.5}Sr_{0.5}Co_{2-x}Fe_xO_{5+\delta}$ samples for different iron content (x = 0, 0.25, 0.5, 0.75, and 1.0) are shown in Figure 1(a) and structural data are given in Table 2. The XRD patterns indicate that all $SmBa_{0.5}Sr_{0.5}Co_{2-x}Fe_xO_{5+\delta}$ specimens are a single-phase perovskite without any detectable impurity phases. The Rietveld refinement data reveal that the diffraction patterns of all samples can be indexed to a tetragonal structure (space group: *P4/mmm*),[23] with those samples being an ordered perovskite structure. The data in Table 2 indicate that the lattice parameters and the unit cell volume of the $SmBa_{0.5}Sr_{0.5}Co_{2-x}Fe_xO_{5+\delta}$ samples increase with increasing Fe content, because the cell volume of the samples with B-site substitution depends on the size of the substituting cations. Comparing the ionic radius of the substituting cations, the crystal ionic radius of iron (r_{Fe3+} = 0.785 Å, CN = 6, and HS) is larger than that of cobalt (r_{Co3+} = 0.75 Å, CN = 6, and HS),[24] which explains the increased volume of the Fe doped SBSCO. As an example depicting the refinement of SBSCF50, Figure 1(b) shows the observed XRD data, the calculated profile, and the difference between them. Rietveld refinement fitting results show excellent agreement between the experimental data and the calculated profile with high reliability factors of R_{wp} = 4.8 %, and R_p = 3.8 % for the pattern with a goodness-of-fit of 1.277.

In order to confirm the phase stability of SBSCF50 at the operating conditions of a SOFC cathode, *in-situ* X-ray diffraction measurements were carried out in a temperature range of 100 - 800 ^oC with steps of 100 ^oC under ambient air and the results are presented in Figure 1(c). SBSCF50 is a single phase perovskite structure without other phases in the entire temperature range of measurements, indicating that it is thermally stable. Figure 1(d) shows the increase of the cell volume as the temperature was increased from 100 to 800 ^oC, determined by *in-situ* X-ray diffraction measurement.

The shift of the peaks to lower 2θ values with increasing temperature indicates thermal expansion. The thermal expansion coefficient (TEC) of SBSCF50 is 19.56 x 10^{-6} K^{-1} calculated from *in-situ* X-ray diffraction patterns; this value is lower than that (22.41 x 10^{-6} K^{-1}) of SBSCO similar to (20-25 x 10^{-6} K^{-1}) of other cobalt containing layered perovskites.[25,26]

Figure 2(a) is a high-angle annular dark field (HAADF) STEM image and selective area electron diffraction (SAED) pattern obtained in the region marked with a white dotted line. The ED pattern clearly shows an ordered superlattice structure through an additional diffraction spot indexed with (001) of a tetragonal structure (lattice constants of a = 3.871 Å and c = 7.757 Å). In addition, the high-resolution STEM image (Figure 2(b)) also confirms an ordered stacking sequence [Ba(Sr)O]-[Co(Fe)O_2]-[SmO_δ]-[Co[Fe]O_2]-[Ba(Sr)O] of the structure, showing atomic Z-contrast between Sm and Ba(Sr) columns.

Scanning electron microscopy (SEM) was carried out to examine the morphology of the $SmBa_{0.5}Sr_{0.5}Co_{2-x}Fe_xO_{5+\delta}$-GDC composites ($x$ = 0, 0.25, 0.5, 0.75, and 1.0). Figure 3(a) shows a cross-sectional SEM image of SBSCF50-GDC|GDC|NiO-GDC with an overview of the three layers, showing a thickness of approximately 15-μm for the cathode and 20-μm for the electrolyte. The interface between the cathode and electrolyte appears to be well-connected and the electrolyte is dense with no pores or cracks. More detailed microstructural images of $SmBa_{0.5}Sr_{0.5}Co_{2-x}Fe_xO_{5+\delta}$-GDC composite cathodes (x = 0, 0.25, 0.5, 0.75, and 1.0) fabricated by the screen printing method are displayed in Figures 3(b)-(f). The cathode has a porous and homogeneous microstructure, which will result in fast transport of gases and highly activated electro-catalytic reactions. Moreover, the microstructure of all $SmBa_{0.5}Sr_{0.5}Co_{2-x}Fe_xO_{5+\delta}$-GDC composite cathodes (x = 0, 0.25, 0.5, 0.75, and 1.0) is similar, and thus this factor appears to be insensitive to Fe substitution.

Figure 4 shows the variation of the oxygen content in the SBSCF system with temperature in air. These curves were derived using initial oxygen content values determined by iodometric titration and the TGA data. All the SBSCF samples start to lose oxygen at T > 200 ^oC. The data in Figure 4 reveal that the degree of oxygen loss decreases with increasing Fe content. The decrease in oxygen loss with Fe doping suggests stronger binding of the oxygen to the lattice with increasing Fe. This is consistent

with a higher standard Gibbs free energy of formation for Fe_3O_4 (-1017.438 kJmol^{-1}) compared to that for Co_3O_4 (-794.871 kJmol^{-1}), implying a stronger Fe-O bond compared to the Co-O bond.[27]

The temperature dependence of the electrical conductivity for $SmBa_{0.5}Sr_{0.5}Co_{2-x}Fe_xO_{5+\delta}$ (x = 0, 0.5, and 1.0) in air is presented in Figure 5. All of the $SmBa_{0.5}Sr_{0.5}Co_{2-x}Fe_xO_{5+\delta}$ (x = 0, 0.5, and 1.0) sample achieve their respective maximums at a range of 400-500 ^oC, and then decrease as the temperature is increased further, exhibiting typical semiconductor behavior. The $SmBa_{0.5}Sr_{0.5}Co_{2-x}Fe_xO_{5+\delta}$ (x = 0, 0.5, and 1.0) samples show a decrease in electrical conductivity with increasing temperature at T>200 ^oC due to oxygen loss from the lattice at higher temperature, as indicated by the TGA data (Figure 4). This can be explained by the fact that the holes are the majority charge carriers and hole-conductivity in cobaltites is usually related to the presence of Co^{4+} ions. The loss of oxygen atoms with increasing temperature not only decreases the hole concentration but also disturbs the (Co,Fe)-O-(Co,Fe) periodic potential and introduces hole localization.[28,29] This can be explained by the preferential formation of Fe^{4+}over Co^{4+} for electronic charge compensation.

At a given temperature, the electrical conductivity decreases with increasing Fe content in $SmBa_{0.5}Sr_{0.5}Co_{2-x}Fe_xO_{5+\delta}$. The oxygen and Co^{4+} ion content in the $SmBa_{0.5}Sr_{0.5}Co_{2-x}Fe_xO_{5+\delta}$ samples decreases with increasing Fe content. This leads to a reduction of the carrier concentration, resulting in a decrease of electrical conductivity. Furthermore, the covalency of the Fe^{4+}-O bond is lower than that of the Co^{4+}-O bond, implying increased electron localization and decreased electrical conductivity with increasing Fe content.[30]

In general, the cathode is in a reduced condition at $p(O_2)$ lower than 0.21 atm due to the cathodic polarization under fuel cell operating conditions.[31] Therefore, both higher redox stability and sufficient electrical conductivity at relatively low $p(O_2)$ are important factors for efficient current collection and long-term stability of the cathode performance for IT-SOFCs at operating conditions.[18,32] Characterization of the basic redox properties is therefore essential, especially under circumstances where the cathode is subjected to relatively low oxygen partial pressures. Basic redox properties including the electrical conductivity and the oxygen nonstoichiometry are also investigated in this study through a specially designed coulometric titration zig for simultaneous measurement of

both properties, which has been explained in detail elsewhere.[20] The $p(O_2)$ dependence of the 4-probe electrical conductivities for $SmBa_{0.5}Sr_{0.5}Co_{2-x}Fe_xO_{5+\delta}$ (x = 0, 0.5, and 1.0) at 700 ^oC is displayed in Figure 6(a). The electrical conductivities of each sample at a given temperature increased with increasing $p(O_2)$, indicating of a typical p-type conductor. The electrical conductivities of $SmBa_{0.5}Sr_{0.5}Co_{2-x}Fe_xO_{5+\delta}$ are within a range of 20 to 550 Scm^{-1} under relatively low oxygen partial pressures, which are typical operating conditions of IT-SOFC cathodes.

Figure 6(b) shows the equilibrium oxygen nonstoichiometries for $SmBa_{0.5}Sr_{0.5}Co_{2-x}Fe_xO_{5+\delta}$ determined by coulometric titration as a function of $p(O_2)$ at 700 ^oC. The initial oxygen content of all samples is determined by iodometric titration and TGA data in air at 700 ^oC, as seen in Table 2. The oxidation isotherms of $SmBa_{0.5}Sr_{0.5}Co_{2-x}Fe_xO_{5+\delta}$ at 700 ^oC have similar shapes, suggesting that the oxidation/reduction mechanisms of all materials are quite similar. SBSCO and SBSCF50 samples start to decay at a $p(O_2)$ of approximately 10^{-5} atm and appear to decompose between 10^{-5} and 10^{-6} atm, while SBSCF100 starts to decay at 10^{-4} atm and appear to also decompose at 10^{-4} atm. A steep decrease of the slope near 10^{-6} atm and 700 ^oC implies that the operating $p(O_2)$ of SBSCF50 should be carefully reviewed considering the structural instability predicted from the redox behavior,[31] which also has been reported in previous studies.[10] The decomposition of SBSCF50 starts at lower $p(O_2)$ as compared with that of SBSCO and SBSCF100, indicating that SBSCF50 has higher redox stability or better durability under cathodic polarization and, consequently, a favourable property for practical application in IT-SOFCs.

Figure 7 presents depth profiles of ^{18}O in SBSCO, SBSCF50 and SBSCF100, which are annealed at 590 ^oC in 200 mbar $^{18}O_2$. The normalized $^{18}O_2$ concentration of the samples was not completely homogeneous for the measured surface areas. The non-uniformity of the $^{18}O_2$ distribution may originate from differences in surface terminations and/or different grain orientations. By integrating the area of the image along the x direction, the normalized values of the $^{18}O_2$ concentration along y can be calculated and fitted to Crank's solution. The obtained fitted values of D^* and k are presented in Figure 7(b). The D^* values of $SmBa_{0.5}Sr_{0.5}Co_{2-x}Fe_xO_{5+\delta}$ (x = 0, 0.5, and 1.0) are 0.75±0.04, 1.71±0.06, and 1.73±0.06 × 10^{-8} cm^2S^{-1}, respectively, confirming that Fe doping has a favorable effect

on the oxygen bulk diffusion properties. In addition, the *k* value of SBSCF50 is higher than those of SBSCO and SBSCF100, and the *k* values of $SmBa_{0.5}Sr_{0.5}Co_{2-x}Fe_xO_{5+\delta}$ (x = 0, 0.5, and 1.0) are 2.2±0.1, 3.4±0.3, and 2.85±0.05 × 10^{-7} cmS^{-1}, respectively. Generally, the oxygen vacancy play a role as the oxygen ion diffusion pathway within the bulk material in simple perovskite system, such as $Ba_{0.5}Sr_{0.5}Co_{0.8}Fe_{0.2}O_{3-\delta}$, $La_{0.6}S_{0.4}C_{0.2}Fe_{0.8}O_{3-\delta}$, and $SrNb_{0.1}Co_{0.7}Fe_{0.2}O_{3-\delta}$.[9,10,33] In the case of layered perovskite system, whereas, pore channels for ion motion in the [Ln-O] and [Co(Fe)-O] planes could provide fast paths for oxygen transport. It is proposed that oxygen ion diffusion paths follow a zig-zag type trajectory through the Co(Fe)-O plane perpendicular to the Ln-O plane. The population of mobile oxygen species may relate to the enhanced oxygen bulk diffusion and surface exchange, that is, higher concentration of mobile oxygen species in the Ln-O layer can lead to faster oxygen kinetics and better electrochemical performance.[13] According to the Adler-Lane-Steele (ALS) model, the area specific resistance (ASR) is related to oxygen kinetics, such as the bulk diffusion (D_o^*) and surface exchange (k_o^0).[34] Under the assumption that the parameters of the microstructure, such as the porosity, cathode surface area, and tortuosity, are similar, high bulk diffusion and surface exchange lead to lower ASR values. Therefore, SBSCF50 is expected to provide fast oxygen diffusion in the bulk and high surface kinetics on the surface of the electrode among the $SmBa_{0.5}Sr_{0.5}Co_{2-x}Fe_xO_{5+\delta}$ (x = 0, 0.5, and 1.0) samples.

The ASR of $SmBa_{0.5}Sr_{0.5}Co_{2-x}Fe_xO_{5+\delta}$ is obtained by AC impedance spectroscopy for $SmBa_{0.5}Sr_{0.5}Co_{2-x}Fe_xO_{5+\delta}$-GDC|GDC|$SmBa_{0.5}Sr_{0.5}Co_{2-x}Fe_xO_{5+\delta}$-GDC symmetrical cells. The ASR value is determined by the impedance intercept between high-frequency and low-frequency with the real axis of the Nyquist plot, which can be expressed as the sum of the charge-transfer resistances and non-charge transfer processes. In the Nyquist plots, the high frequency arcs are equivalent to R_2, which is related to charge transfer during the migration and diffusion of oxygen ions from the triple-phase boundary (TPB) into the electrolyte. Meanwhile, the low frequency arcs correspond to R_3, which is attributed to non-charge-transfer processes including oxygen surface exchange, solid-state diffusion, and gas-phase diffusion inside and outside the electrode.[34] The experimental impedance

spectroscopy patterns are shown in figure 8(a) and are well fitted by the equivalent circuit model presented as an inset in Fig. 8 (a). The inset in Figure 8(a) shows the R_2 and R_3 at various Fe content determined from the impedance spectra. The experimental R_2 and R_3 values of $SmBa_{0.5}Sr_{0.5}Co_{2-x}Fe_xO_{5+\delta}$ (x = 0, 0.25, 0.5, 0.75, and 1.0)-GDC based on a GDC symmetrical cell decrease with Fe content up to x = 0.5, and the $R_p(=R_2+R_3)$ values of $SmBa_{0.5}Sr_{0.5}Co_{2-x}Fe_xO_{5+\delta}$ (x = 0, 0.25, 0.5, 0.75, and 1.0)-GDC are 0.141, 0.101, 0.081, 0.104, and 0.136 Ω cm^2 at 600 °C, respectively. In general, the population of mobile oxygen species in layered perovskites may contribute to enhanced oxygen kinetics associated with oxygen bulk diffusion and surface exchange.[36] A higher concentration of mobile oxygen species in the Sm-O layer due to larger amount of Fe doping (up to ~50%) may lead to faster oxygen kinetics and better electrochemical performance.[13] Therefore, among the $SmBa_{0.5}Sr_{0.5}Co_{2-x}Fe_xO_{5+\delta}$ samples, SBSCF50 is expected to provide fast oxygen diffusion in the bulk and high surface kinetics on the surface of the electrode.

Arrhenius plots of the ASR for $SmBa_{0.5}Sr_{0.5}Co_{2-x}Fe_xO_{5+\delta}$ are shown in Figure 8(b). The activation energy is directly related to the cathode properties including the oxygen adsorption, dissociation, and surface/bulk diffusion.[36,37] The activation energies of $SmBa_{0.5}Sr_{0.5}Co_{2-x}Fe_xO_{5+\delta}$ are calculated from the Arrhenius plots of the fitted line. The activation energy of $SmBa_{0.5}Sr_{0.5}Co_{2-x}Fe_xO_{5+\delta}$ (x = 0.25, 0.5, and 0.75) is around 106 kJ mol^{-1} and those samples exhibit lower activation energy than $SmBa_{0.5}Sr_{0.5}Co_{2-x}Fe_xO_{5+\delta}$ (x = 0 and 1.0).

To evaluate the performance of $SmBa_{0.5}Sr_{0.5}Co_{2-x}Fe_xO_{5+\delta}$ cathode materials in a practical fuel cell, we used anode-supported cells based on a 15-μm-thick GDC electrolyte. Figure 9 shows the power density and cell voltage as a function of the current density for the $SmBa_{0.5}Sr_{0.5}Co_{2-x}Fe_xO_{5+\delta}$ (x = 0, 0.5, and 1.0)-GDC|GDC|NiO-GDC cells using humidified H_2 (3 % H_2O) as a fuel and ambient air as an oxidant in a temperature range of 500 - 650 °C. The maximum power density of SBSCO, SBSCF50, and SBSCF100 is 2.03, 2.19, and 1.81 W cm^{-2} at 650 °C and 1.38, 1.56, and 1.28 W cm^{-2} at 600 °C, respectively. The single cell performance improves with increasing Fe content up to x = 0.5 in the $SmBa_{0.5}Sr_{0.5}Co_{2-x}Fe_xO_{5+\delta}$ oxides, while SBSCF100 shows a sudden reduction of cell performance,

consistent with the trend of the ASR and electrical conductivity results.

In conclusion, SBSCF50 is a promising material as a cathode for IT-SOFCs with Fe substitution in SBSCO enhancing the performance and redox stability, and it also shows satisfactory electrical properties and electrochemical performance under typical fuel cell operating conditions.

Conclusion

In this study, we focus on the catalytic effect of Fe doping into $SmBa_{0.5}Sr_{0.5}Co_{2-x}Fe_xO_{5+\delta}$ for the oxygen reduction reaction (ORR) and optimize the amount of Fe substitution by investigating the structural characteristics, electrical properties, redox properties, oxygen kinetics, and electrochemical performance of $SmBa_{0.5}Sr_{0.5}Co_{2-x}Fe_xO_{5+\delta}$ (x = 0, 0.25, 0.5, 0.75, and 1.0) in terms of application as an intermediate-temperature solid oxide fuel cell (IT-SOFC) cathode material. SBSCF50 shows higher redox stability at lower $p(O_2)$ compared with that of SBSCO and SBSCF100 from the coulometric titration results. Furthermore, it exhibits lower ASR values of 0.081 $\Omega\,cm^2$ and excellent cell performance of 1.56 W cm^{-2} at 600 ^oC. Its enhanced electrical performance is ascribed to fast oxygen diffusion in the bulk and high surface kinetics from the depth profile of normalized isotope oxygen fraction. SBSCF50 provides a combination of fast oxygen diffusion and high surface kinetics, and also shows enhanced redox stability and electrochemical performance under typical fuel cell operating conditions. SBSCF50 is indeed a promising material as a cathode for IT-SOFC systems.

Acknowledgements

This research was supported by the Mid-career Researcher Program (2013R1A2A2A04015706) funded by the Korea Government Ministry of Science, ICT and Future Planning and the Basic Science Research Program (2010-0021214) funded by the Ministry of Education through the National Research Foundation of Korea. It was also supported by Development Program of the Korea Institute of Energy Research (KIER) (B5-2422) and the Dong-Eui University Grant (2014AA107).

References

[1] M. D. Gross, J. M. Vohs, and R. J. Gorte, *J. Mater. Chem.*, 2007, **17**, 3071.

[2] S. Sengodan, S. Choi, A. Jun, T. H. Shin, Y. W. Ju, H. Y. Jeong, J. Shin, J. T. S. Irvine, and G. Kim, *Nat. Mater.*, 2015, **14**, 205.

[3] F. Dong, M. Ni, Y. Chen, D. Chen, M. O. Tadé, and Z. Shao, *J. Mater. Chem. A*, 2014, **2**, 20520.

[4] B. C. H. Steele and A. Heinzel, *Nature*, 2001, **414**, 345.

[5] S. Yoo, A. Jun, Y. -W. Ju, D. Odkhuu, J. Hyodo, H. Y. Jeong, N. Park, J. Shin, T. Ishihara, and G. Kim, *Angew. Chem. Int. Ed.*, 2014, **53**, 13064.

[6] W. Jung, K. L. Gu, Y. Choi, and S. M. Haile, *Energy Environ. Sci.*, 2014, **7**, 1685.

[7] S. B. Adler, J. A. Lane, and B. C. H. Steele, *J. Electrochem. Soc.*, 1996, **143**, 3554.

[8] P. Ried, P. Holtappels, A. Wichser, A. Ulrich, and T. Graule, *J. Electrochem. Soc.*, 2008, **155**, B1029.

[9] Z. Shao and S. M. Haile, *Nature*, 2004, **431**, 170.

[10] A. Jun, S. Yoo, O. -H. Gwon, J. Shin, and G. Kim, *Electrochim. Acta*, 2013, **89**, 372.

[11] S. Park, S. Choi, J. Shin, and G. Kim, *J. Power Sources*, 2010, **210**, 172.

[12] C. Xia, W. Rauch, F. Chen, and M. Liu, *Solid State Ionics*, 2002, **149**, 11.

[13] S. Choi, S. Yoo, J. Kim, S. Park, A. Jun, S. Sengodan, J. Kim, J. Shin, H. Y. Jeong, Y. Choi, G. Kim, and M. Liu, *Sci. Rep.*, 2013, **3**, 2426.

[14] A. Jun, J. Kim, J. Shin, and G. Kim, *Int. J. Hydrogen Energy*, 2012, **37**, 18381.

[15] T. Broux, M. Bahout, J. M. Hanlon, O. Hernandez, S. Paofai, A. Berenov, and S. J. Skinner, *J. Mater. Chem. A*, 2014, **2**, 17015.

[16] S. Park, S. Choi, J. Shin, and G. Kim, *RSC Adv.*, 2014, **4**, 1775.

[17] J. Kim, S. Choi, A. Jun, H. Y, Jeong, J. Shin, and G. Kim, *ChemSusChem*, 2014, **7**, 1669.

[18] A. Jun, J. Shin, and G. Kim, *Phys. Chem. Chem. Phys.*, 2013, **15**, 19906.

[19] D. S. Tsvetkov, I. L. Urusov, A. Y. Zuev, *Thermochim. Acta*, 2011, **519**, 12.

[20] S. Yoo, J. Y. Shin, and G. Kim, *J. Mater. Chem.*, 2011, **21**, 439.

[21] R. A. De Souza, R. J. Chater, *Solid State Ionics*, 2005, **176**, 1915.

[22] J. Crank, *The Mathematics of Diffusion*, Oxford Univ. Press, London, 2nd edn., 1975.

[23] A. Maignan, C. Martin, D. Pelloquin, N. Nguyen, and B. Raveau, *J. Solid State Chem.*, 1999, **142**, 247.

[24] R. D. Shannon, *Acta. Cryst.*, 1976, **A32**, 751.

[25] J. H. Kim, M. Cassidy, J. T. S. Irvine, and J. -M. Bae, *J. Electrochem. Soc.*, 2009, **156**, B682.

[26] S. Park, S. Choi, J. Shin, and G. Kim, *Electrochim. Acta*, 2014, **125**, 683.

[27] M. W. Chase Jr., C. A. Davies, J. R. Downey Jr., D. J. Frurip, R. A. McDonald, and A. N. Syverud*, J. Phys. Chem. Ref. Data 118 (Suppl. 1)*, 1985, 926.

[28] K. T. Lee and A. Manthiram, *Chem. Mater.*, 2006, **18**, 1621.

[29] H. Takahashi, F. Munakata, and M. Yamanaka, *Physical Review B*, 1998, **57**, 15211.

[30] Y. N. Kim, J. –H. Kim, and A. Manthiram, *J. Power Sources*, 2010, **195**, 6411.

[31] S. B. Adler, *Chem. Rev.*, 2004, **104**, 4791.

[32] D. M. Bastidas, S. Tao, and J. T. S. Irvine, *J. Mater. Chem.*, 2006, **16**, 1603.

[33] Y. Zhu, J. Sunarso, W. Zhou, S. Jiang, and Z. Shao, *J. Mater. Chem. A*, 2014, **2**, 15454.

[34] S. B. Adler, J. A. Lane, and B. C. H. Steele, *J. Electrochem. Soc.*, 1996, **143**, 3554.

[35] M. Bevilacqua, T. Montini, C. Tavagnacco, E. Fonda, P. Fornasiero, and M. Graziani, *Chem. Mater.*, 2007, **19**, 5926.

[36] G. Kim, S. Wang, A. J. Jacobson, L. Reimus, P. Brodersen, and C. A. Mims, *J. Mater. Chem.*, 2007, **17**, 2500.

[37] S. Lü, X. Meng, Y. Ji, C. Fu, C. Sun, H. Zhao, *J. Power Sources*, 2010, **195**, 8094.

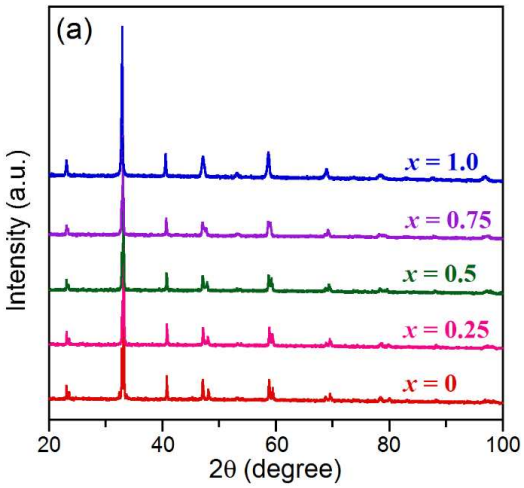

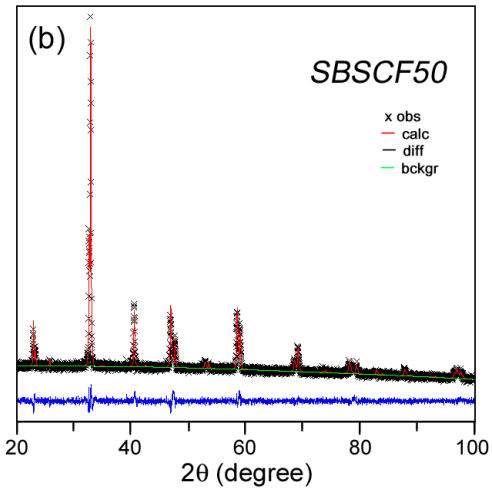

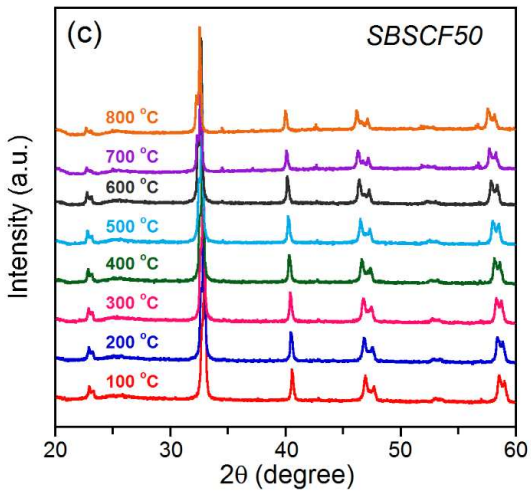

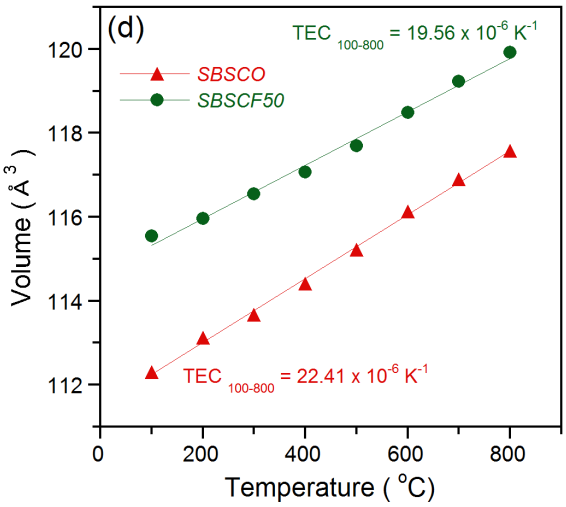

Figure 1. (a) XRD patterns of $SmBa_{0.5}Sr_{0.5}Co_{2-x}Fe_xO_{5+\delta}$ (x = 0, 0.25, 0.5, 0.75, and 1.0) powders. (b) Observed and calculated XRD profiles and the difference between them for $SmBa_{0.5}Sr_{0.5}Co_{1.5}Fe_{0.5}O_{5+\delta}$. (c) *In-situ* X-ray diffraction patterns for $SmBa_{0.5}Sr_{0.5}Co_{1.5}Fe_{0.5}O_{5+\delta}$ in air from 100 to 800 °C. (d) Dependence of unit cell volume V (Å ^{3}) on temperature from *in-situ* X-ray diffraction patterns for $SmBa_{0.5}Sr_{0.5}Co_{2-x}Fe_xO_{5+\delta}$ (x = 0 and 0.5).

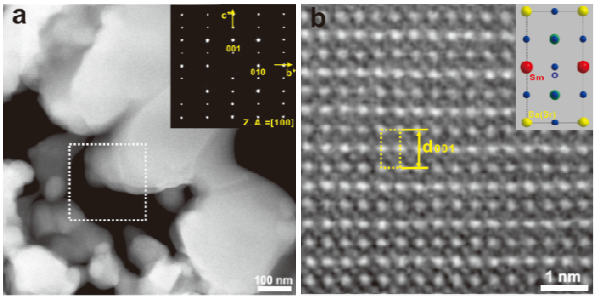

Figure 2. (a) High-angle annular dark field (HAADF) STEM image and corresponding selective-area electron diffraction (SAED) pattern obtained from an as-synthesized $SmBa_{0.5}Sr_{0.5}Co_{1.5}Fe_{0.5}O_{5+\delta}$ sample. (b) A high-resolution HAADF STEM image of the grain marked with a white rectangle in (a). The crystal structure of ordered $SmBa_{0.5}Sr_{0.5}Co_{1.5}Fe_{0.5}O_{5+\delta}$ is represented in the right inset.

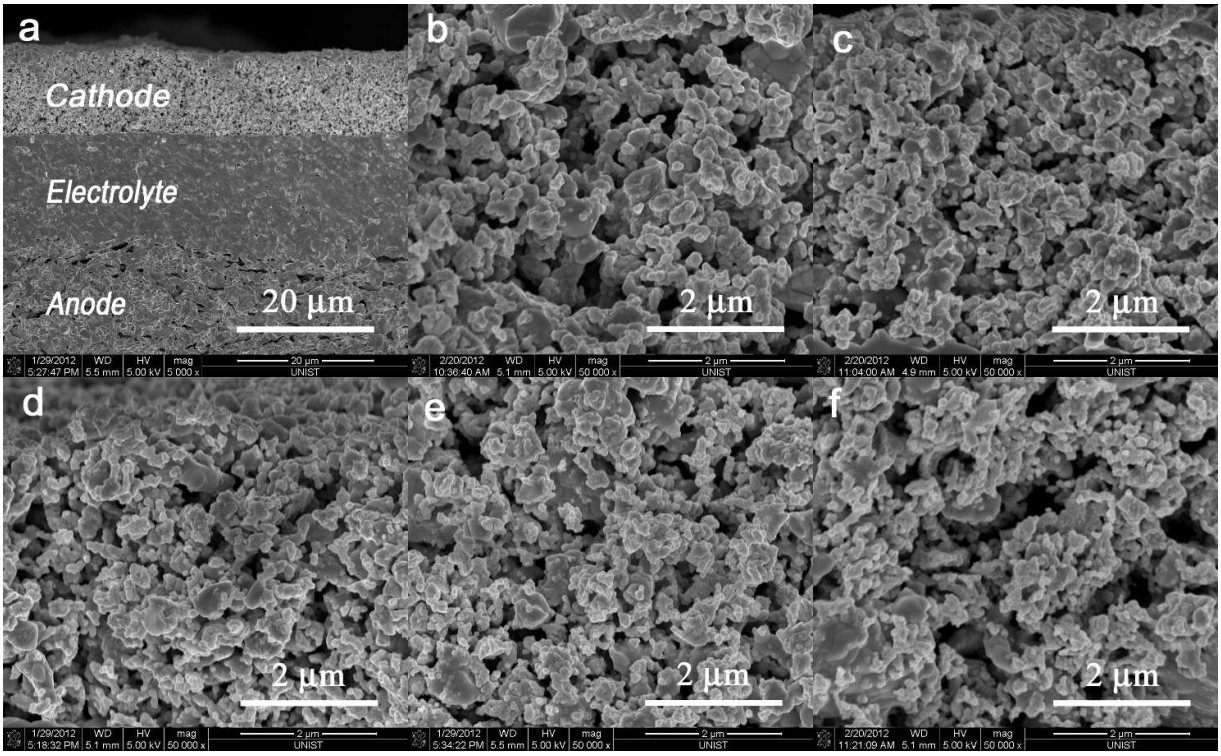

Figure 3. Scanning electron microscopy images of $SmBa_{0.5}Sr_{0.5}Co_{2-x}Fe_xO_{5+\delta}$ (x = 0, 0.25, 0.5, 0.75, and 1.0)-GDC cathodes: (a) a cross section consisting of the dense GDC electrolyte with the porous $SmBa_{0.5}Sr_{0.5}Co_{1.5}Fe_{0.5}O_{5+\delta}$-GDC composite cathode and NiO-GDC anode; (b)-(f) microstructure of $SmBa_{0.5}Sr_{0.5}Co_{2-x}Fe_xO_{5+\delta}$ (x = 0, 0.25, 0.5, 0.75, and 1.0)-GDC cathodes fabricated using screen printing followed by sintering at 950 ^{o}C for 4 hours.

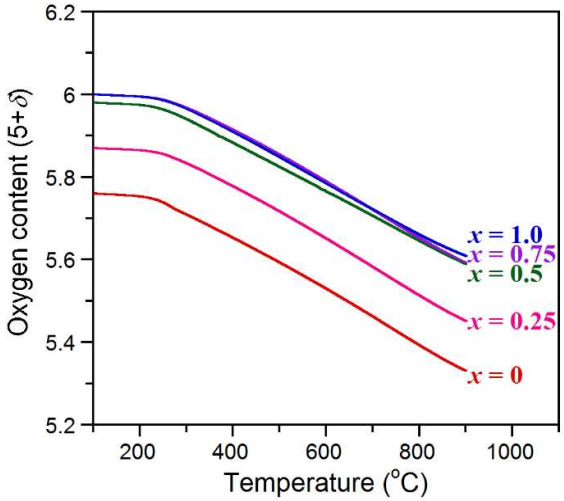

Figure 4. Variations of oxygen contents in $SmBa_{0.5}Sr_{0.5}Co_{2-x}Fe_xO_{5+\delta}$ (x = 0, 0.25, 0.5, 0.75, and 1.0) with temperature in air.

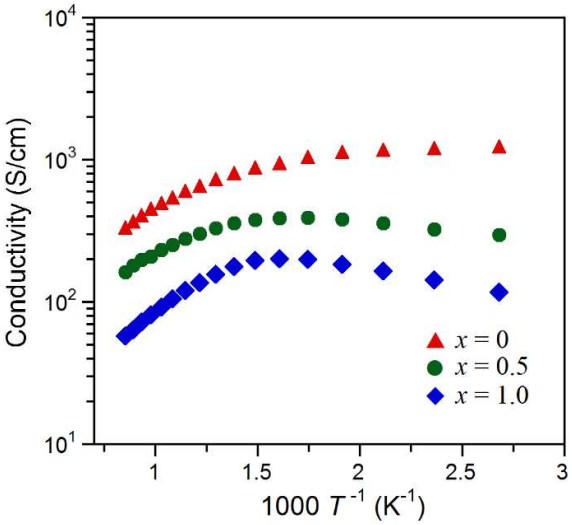

Figure 5. Electrical conductivities of $SmBa_{0.5}Sr_{0.5}Co_{2-x}Fe_xO_{5+\delta}$ (x = 0, 0.5, and 1.0) at various temperatures from 100 to 750 ^{o}C in air.

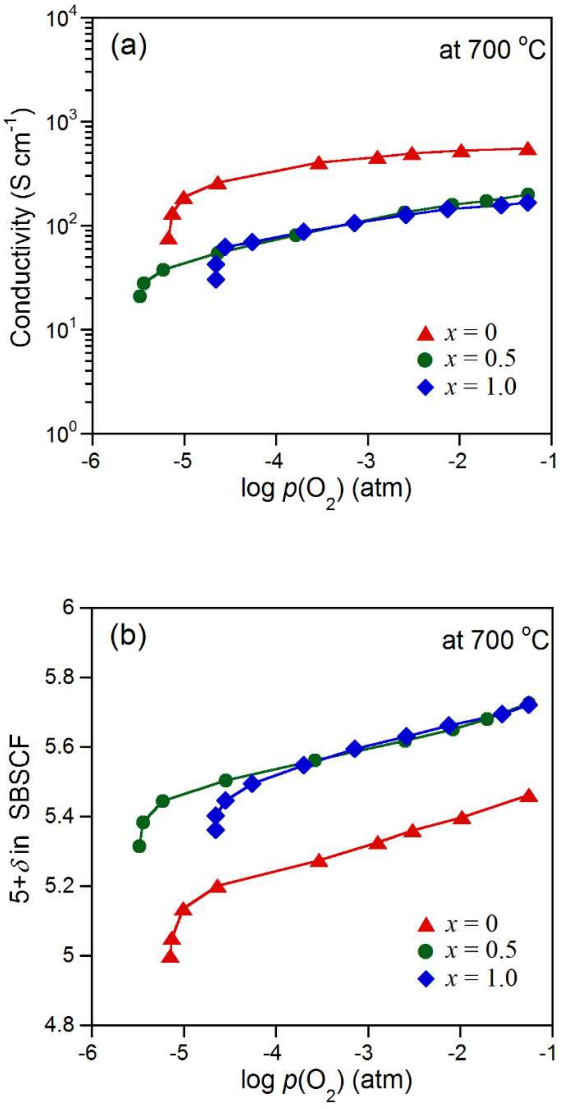

Figure 6. (a) Electrical conductivity of $SmBa_{0.5}Sr_{0.5}Co_{2-x}Fe_xO_{5+\delta}$ (x = 0, 0.5, and 1.0) and (b) Oxidation isotherms $SmBa_{0.5}Sr_{0.5}Co_{2-x}Fe_xO_{5+\delta}$ (x = 0, 0.5, and 1.0) in various $p(O_2)$ at 700 °C.

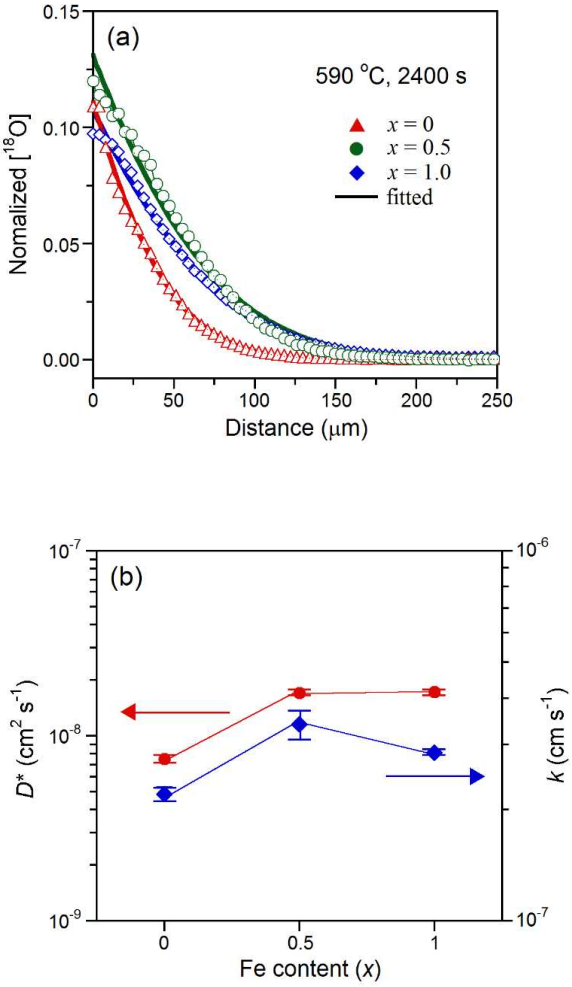

Figure 7. (a) Depth profile of normalized isotope oxygen fraction in $SmBa_{0.5}Sr_{0.5}Co_{2-x}Fe_xO_{5+\delta}$ (x = 0, 0.5, and 1.0) exchanged at 590 °C for 2400 sec, obtained by linescan measurement. The symbols and solid line show the measured results and fitted results, respectively. (b) D^* and k fitted values for various values of Fe content obtained from the depth profile of the normalized isotope oxygen fraction.

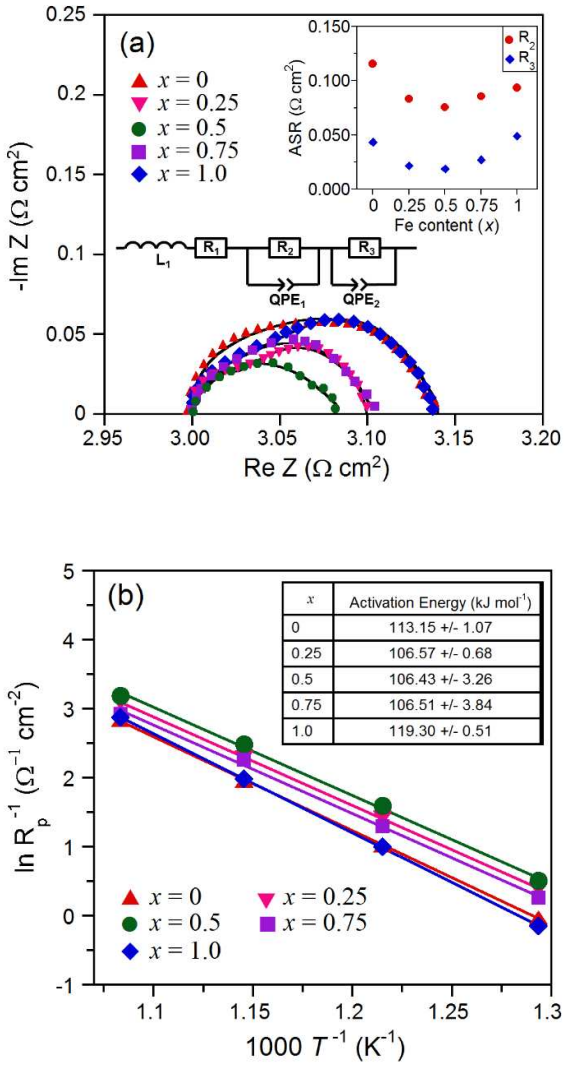

Figure 8. Experimental and simulated impedance plots of (a) $SmBa_{0.5}Sr_{0.5}Co_{2-x}Fe_xO_{5+\delta}$ (x = 0, 0.25, 0.5, 0.75, and 1.0)-GDC at 600 °C by the equivalent circuit shown as an inset. The inset in (a) shows the R_2 and R_3 at various Fe content determined from the impedance spectra. Arrhenius plots of 1/ASR and activation energy of (b) $SmBa_{0.5}Sr_{0.5}Co_{2-x}Fe_xO_{5+\delta}$-GDC.

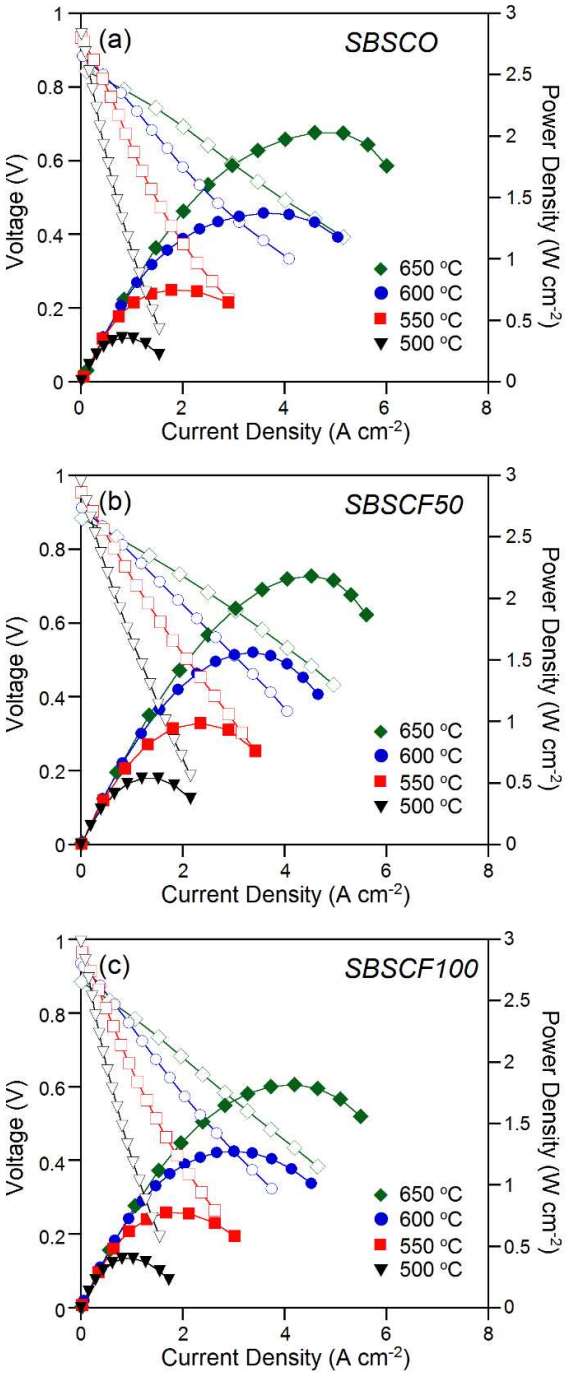

Figure 9. *I-V* polarization curves and the corresponding power densities of the test cells with (a), $SmBa_{0.5}Sr_{0.5}Co_2O_{5+\delta}$ -GDC (b), $SmBa_{0.5}Sr_{0.5}Co_{1.5}Fe_{0.5}O_{5+\delta}$ -GDC (c), $SmBa_{0.5}Sr_{0.5}CoFeO_{5+\delta}$ -GDC as the cathodes, using humidified H_2 (3% H_2O) as a fuel and static ambient air as an oxidant in a temperature range of 500 - 650 °C.

Table 1. **Abbreviations of specimens.**

Chemical composition	Abbreviations
$Ce_{0.9}Gd_{0.1}O_{2-\delta}$	GDC
$SmBa_{0.5}Sr_{0.5}Co_2O_{5+\delta}$	SBSCO
$SmBa_{0.5}Sr_{0.5}Co_{1.75}Fe_{0.25}O_{5+\delta}$	SBSCF25
$SmBa_{0.5}Sr_{0.5}Co_{1.5}Fe_{0.5}O_{5+\delta}$	SBSCF50
$SmBa_{0.5}Sr_{0.5}Co_{1.25}Fe_{0.75}O_{5+\delta}$	SBSCF75
$SmBa_{0.5}Sr_{0.5}CoFeO_{5+\delta}$	SBSCF100

Table 2. Space group and lattice parameters of $SmBa_{0.5}Sr_{0.5}Co_{2-x}Fe_xO_{5+\delta}$.

	Space group	*a* (Å)	*b* (Å)	*c* (Å)	*V* (Å)^3	Oxygen content (5+δ)	Oxidation state (Co,Fe)
SBSCO	*P4/mmm*	3.862	3.862	7.571	112.921	5.76	3.26
SBSCF25	*P4/mmm*	3.863	3.863	7.759	113.354	5.87	3.37
SBSCF50	*P4/mmm*	3.866	3.866	7.616	113.809	5.98	3.48
SBSCF75	*P4/mmm*	3.870	3.870	7.653	114.612	6.00	3.50
SBSCF100	*P4/mmm*	3.870	3.870	7.695	115.247	6.00	3.50

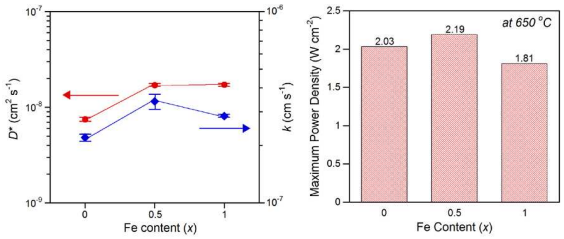

The optimal Fe substitution, $SmBa_{0.5}Sr_{0.5}Co_{1.5}Fe_{0.5}O_{5+\delta}$, enhanced the performance and redox stability due to its fast oxygen kinetics.